



HAL
open science

Basic constraints for design optimization of cubic and bistable NES

Zhenhang Wu, Sébastien Seguy, Manuel Paredes

► **To cite this version:**

Zhenhang Wu, Sébastien Seguy, Manuel Paredes. Basic constraints for design optimization of cubic and bistable NES. *Journal of Vibration and Acoustics*, 2022, 144 (2), pp.021003. 10.1115/1.4051548 . hal-03273247

HAL Id: hal-03273247

<https://hal.insa-toulouse.fr/hal-03273247>

Submitted on 29 Jun 2021

HAL is a multi-disciplinary open access archive for the deposit and dissemination of scientific research documents, whether they are published or not. The documents may come from teaching and research institutions in France or abroad, or from public or private research centers.

L'archive ouverte pluridisciplinaire **HAL**, est destinée au dépôt et à la diffusion de documents scientifiques de niveau recherche, publiés ou non, émanant des établissements d'enseignement et de recherche français ou étrangers, des laboratoires publics ou privés.

Basic Constraints for Design Optimization of Cubic and Bistable NES

Zhenhang Wu

Institut Clément Ader (ICA), CNRS,
INSA-ISAE-Mines Albi-UPS,
Université de Toulouse,
3 rue Caroline Aigle
Toulouse, F-31400, France
zhenhang.wu@insa-toulouse.fr

Sébastien Seguy

Institut Clément Ader (ICA), CNRS,
INSA-ISAE-Mines Albi-UPS,
Université de Toulouse,
3 rue Caroline Aigle
Toulouse, F-31400, France
sebastien.seguy@insa-toulouse.fr

Manuel Paredes

Institut Clément Ader (ICA), CNRS,
INSA-ISAE-Mines Albi-UPS,
Université de Toulouse,
3 rue Caroline Aigle
Toulouse, F-31400, France
manuel.paredes@insa-toulouse.fr

This work mainly concentrates on the optimization of cubic and bistable NES to find the maximum efficiency point under harmonic excitation. The conservative system is considered to reveal the inner property of the damping system. With the application of the multiple scales method and the complex variables method, the threshold of excitation and different response regimes are distinguished under the assumption of 1:1 resonance. The maximum efficiency point of cubic and bistable NES occurs when SMR disappears. The factors that affect the optimal efficiency limit are explored. The result indicates that the maximum absorption efficiency level is mainly determined by the damping parameters. Compared with the cubic case, the bistable case involves more complex regimes in terms of chaos oscillation. The influence of damping parameters on the chaos threshold is discussed to adopt different energy levels. With the help of analytical predictions, the proper nonlinear stiffness is determined for certain harmonic excitation. This work offers some fundamental insights into the optimal design of cubic and bistable NES.

1 Introduction

The elimination of harmful vibrations is an inevitable issue in the modern manufacturing industry and the civil engineering domain. A classic vibration-absorbing device, called the Tuned Mass Damper (TMD) is widely used [1]. It consists of a mass that is connected, by a linear spring and a damper, to a primary mass. If the linear stiffness is substi-

tuted by a nonlinear one, a novel type of vibration-absorbing device, called a Nonlinear Energy Sink (NES), is obtained. Compared to the TMD, the NES has some remarkable advantages: a lighter attached mass, a broader range of absorption frequencies and the capability to erase the resonance peak [2].

Due to the existence of nonlinearity and damping, the NES can produce a one-way, irreversible Target Energy Transfer (TET) from the primary system to the NES mass, where the energy is finally dissipated by damping [3]. The TET phenomenon can be explained by studying the energy of the system without considering the damping and external force [4]. These special periodic solutions of the conservative system are referred to as Nonlinear Normal Modes (NNM). These stable special orbits are responsible for TET [5]. The efficiency of this mechanism in absorbing vibration has been explored both numerically [6, 7] and experimentally [8–11]. Also, its potential applications in structural seismic control [12] and in mitigating the hypersonic 3-D wing flutter [13] have been studied.

The complex variables method and the multiple scales method are widely used to separate the relaxation-oscillation into fast and slow time scales during the TET [14]. The Slow Invariant Manifold (SIM) structure with respect to the slow time scales manifests the jumping phenomenon between the stable branches and also provides the damping condition required to trigger the Strongly Modulated Response (SMR) [15]. The final periodic response corresponds to the ordinary fixed point of the averaged flow equation in the condition of 1:1 resonance. On the other hand, the appearance of folded

singularities leads to the occurrence of SMR. The stability of SMR is transferred into a 1-D mapping problem, where the drop point after 'jumping' is located in a certain interval of phase portraits. The necessary condition of external harmonic force is also investigated experimentally to trigger the SMR mechanism [11].

If the negative stiffness is added between the primary system and the attached NES mass, the NES mass can possess two stable equilibria and is called a bistable NES. This addition essentially changes the dynamic regimes of the bistable system. So it also requires a different analytical treatment. According to the potential energy surface in the Hamilton system [16], the double-wells distinguish the different energy levels as intra-well oscillation, at low energy input, and inter-well oscillation. If the input energy is intense enough, chaos regimes also occur. The Melnikov method is employed to determine the boundary of the chaos response for the homoclinic bifurcation [17, 18]. Based on the different response regimes, Qiu et al. [19] have developed an optimization process to locate an optimal point in the transition between the SMR and stable periodic response, where the efficiency has achieved the maximum value.

From the perspective of absorbing efficiency, it is necessary to assess the energy flow between the NES and the Linear Oscillator (LO) to evaluate the NES's performance. A novel methodology to visualize various energies is presented for NES in [20]. Wei et al. [21] developed a modified optimal equation to improve the efficiency of NES in pulse excitation with relatively low damping. The numerical verification confirms that the energy dissipation is almost constant with optimal TET under various impulse excitations. The performances of several types of NES, such as bistable NES, piecewise NES, rotary NES and vibro-impact NES are investigated under the initial induced impulse energy in detail [22]. Among them, the enhanced single side vibro-impact NES shows the best performance in reducing the induced impact acceleration. It has been concluded that deeper and more widely separated wells on the potential surface in the case of bistable NES require more input acceleration to produce voltages [23]. The modified bistable NES can absorb input shock energy with high efficiency [24]. A procedure to tune a bistable NES and the effects of parameters that efficiently mitigate oscillation of LO for more than one vibration mode are described [25].

The present article is organized as follows. In Section 2, the conservative systems of cubic and bistable NES are presented. The assumption of 1:1 resonance is applied throughout the paper. The frequency-energy relation is described with its variety of negative stiffness and nonlinear stiffness. In Section 3, the non-conservative system with harmonic force is considered. The asymptotic analysis is developed to distinguish the different regimes by applying the complex variables method and multiple scales method. In Section 4, the initial energy level required to trigger the SMR is combined with the frequency-energy analysis of the conservative system. The efficiency levels alter under a continuously increasing excitation in cubic NES case. The analytical relation between the designed nonlinear stiffness and target ex-

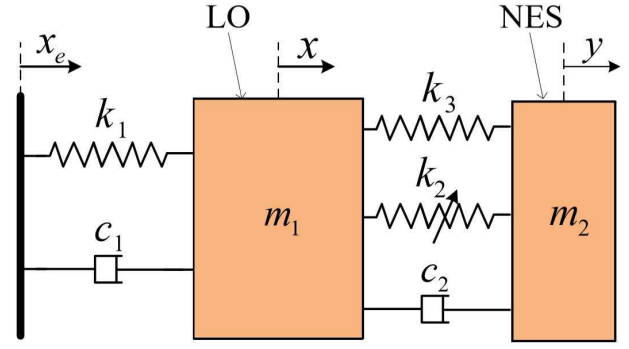


Fig. 1. Schematic of primary structure (LO) and NES system

citations is proposed. The correction coefficient helps the optimal stiffness functions better fit the numerical result. In Section 5, the different potential energy trajectories separate the response regime into four stages in the bistable NES case. The chaos boundary of the damping parameters is studied by Melnikov analysis. The optimal point is found in the transition between the SMR and the stable response. The robustness of the design method facing the uncertainties of K and δ is investigated. The last section mentions some noteworthy conclusions.

2 Frequency-energy analysis for conservative systems

The target system is described schematically in Fig. 1. The LO m_1 is excited harmonically through the linear stiffness k_1 and connected with NES mass m_2 by a linear stiffness k_2 and nonlinear stiffness k_3 . The c_1 and c_2 are the damping of LO and NES respectively. The motion equation is:

$$\begin{aligned} m_1 \ddot{x} + k_1 x + c_1 \dot{x} + c_2 (\dot{x} - \dot{y}) \\ + k_2 (x - y)^3 + k_3 (x - y) = k_1 x_e + c_1 \dot{x}_e \\ m_2 \ddot{y} + c_2 (\dot{y} - \dot{x}) + k_2 (y - x)^3 + k_3 (y - x) = 0 \end{aligned} \quad (1)$$

The harmonic excitation is expressed as $x_e = G \cos(\omega t)$. If the linear stiffness value k_3 is shifted to be zero or negative, equation. (1) can describe the pure cubic and bistable NES. By introducing the variables:

$$\begin{aligned} \varepsilon = \frac{m_2}{m_1}, \omega_0^2 = \frac{k_1}{m_1}, K = \frac{k_2}{m_2 \omega_0^2}, \delta = \frac{k_3}{m_2 \omega_0^2} \\ \lambda_1 = \frac{c_1}{m_2 \omega_0}, \lambda_2 = \frac{c_2}{m_2 \omega_0}, F = \frac{G}{\varepsilon}, \Omega = \frac{\omega}{\omega_0}, \tau = \omega_0 t \end{aligned} \quad (2)$$

the equations of motion can be rewritten as

$$\begin{aligned} \ddot{x} + x + \varepsilon \lambda_1 \dot{x} + \varepsilon \lambda_2 (\dot{x} - \dot{y}) \\ + \varepsilon K (x - y)^3 + \varepsilon \delta (x - y) = \varepsilon F \cos \Omega \tau \\ \varepsilon \ddot{y} + \varepsilon \lambda_2 (\dot{y} - \dot{x}) + \varepsilon K (y - x)^3 + \varepsilon \delta (y - x) = 0 \end{aligned} \quad (3)$$

The main feature of NES is TET. It leads the energy of the primary system to be transferred irreversibly to the NES

and dissipated passively by the damping. The existence of damping (energy dissipation) and nonlinearity is a prerequisite for the TET mechanism [2]. Therefore, TET cannot take place in a conservative system.

The concept of Limiting Phase Trajectory (LPT) in the strongly nonlinear regime is responsible for the strongest possible TET in the weakly dissipative system. The stationary solution on the LPT corresponds to a special 1:1 resonance orbit, where the LO and NES oscillate with identical frequency. In the absence of damping, the 1:1 resonance capture is mainly responsible for intensive energy exchange [16], so the conservative system is still an essential basis for understanding and optimizing the TET mechanism.

To study the features of in-phase (S11+) and out-of-phase (S11-) 1:1 resonance, the frequency-energy plot depicts the main backbone branch of these synchronous period orbits. Initially, by assuming $\lambda_1 = \lambda_2 = 0$, $F = 0$, equation. (3) is converted into the Hamiltonian version. Then the complex variables $\psi_1 e^{i\Omega\tau} = \dot{x} + j\Omega x$ and $\psi_2 e^{i\Omega\tau} = \dot{y} + j\Omega y$ where $j^2 = -1$ are introduced into Eqn. (3). This complexification approach is also applied in [26]. The ψ_i represents the 'slow' complex part variation of amplitude, and the Ω is the 'fast' oscillation of frequency. By averaging over the fast frequency, it gives:

$$\begin{aligned} \psi_1 - \frac{i\delta\epsilon(\psi_1 - \psi_2)}{2\Omega} - \frac{i\psi_1}{\Omega} + \frac{i\Omega\psi_1}{2} + \frac{3iK\epsilon}{8\Omega^3} (\psi_2^2\bar{\psi}_2 - \psi_1^2\bar{\psi}_1 \\ + \psi_1^2\bar{\psi}_2 - \psi_2^2\bar{\psi}_1 - 2\psi_1\psi_2\bar{\psi}_2 + 2\psi_1\bar{\psi}_1\psi_2) = 0 \\ \psi_2 + \frac{i\delta\epsilon(\psi_1 - \psi_2)}{2\Omega} + \frac{i\Omega\psi_2}{2} + \frac{3iK\epsilon}{8\Omega^3} (-\psi_2^2\bar{\psi}_2 + \psi_1^2\bar{\psi}_1 \\ - \psi_1^2\bar{\psi}_2 + \psi_2^2\bar{\psi}_1 + 2\psi_1\psi_2\bar{\psi}_2 - 2\psi_1\bar{\psi}_1\psi_2) = 0 \end{aligned} \quad (4)$$

To study the evolution of amplitude, the polar forms $\psi_1 = A_1 e^{j\alpha_1}$ and $\psi_2 = A_2 e^{j\alpha_2}$ are substituted. The A_1 , A_2 , α_1 and α_2 are real modulations and represent the slow evolution of amplitudes and phases of 1:1 resonance. Obviously, on the periodic solution branch S11±, the condition $\alpha_1 = \alpha_2$ is trivially satisfied according to [16]. Then Eqn. (5) is obtained in the following forms:

$$\begin{aligned} \frac{\Omega A_1}{2} - \frac{\epsilon\delta(A_1 - A_2) + A_1}{2\Omega} - \frac{3}{8} \frac{K\epsilon(A_1 - A_2)^3}{\Omega^3} = 0 \\ \frac{\Omega A_2}{2} + \frac{\epsilon\delta(A_1 - A_2)}{2\Omega} + \frac{3}{8} \frac{K\epsilon(A_1 - A_2)^3}{\Omega^3} = 0 \end{aligned} \quad (5)$$

The approximate response $x(\tau) = (A_1/\Omega)\cos(\Omega\tau)$ and $y(\tau) = (A_2/\Omega)\cos(\Omega\tau)$ can be obtained by solving the above amplitude equation (Eqn. (5)). The amplitude of $x(\tau)$ and $y(\tau)$ are given by: $Y(\Omega) = A_1/\Omega$ and $V(\Omega) = A_2/\Omega$ respectively where:

$$\begin{aligned} A_1 = \frac{2}{3} \frac{\Omega^3 \sqrt{K(\Omega^2\epsilon + \Omega^2 - 1)(\Omega^4 - \Omega^2\delta\epsilon - \Omega^2\delta - \Omega^2 + \delta)} \sqrt{3\epsilon}}{K(\Omega^2\epsilon + \Omega^2 - 1)^2} \\ A_2 = -\frac{2}{3} \frac{\sqrt{3} \sqrt{K(\Omega^2\epsilon + \Omega^2 - 1)(\Omega^4 - \Omega^2\delta\epsilon - \Omega^2\delta - \Omega^2 + \delta)} \Omega(\Omega^2 - 1)}{K(\Omega^2\epsilon + \Omega^2 - 1)^2} \end{aligned} \quad (6)$$

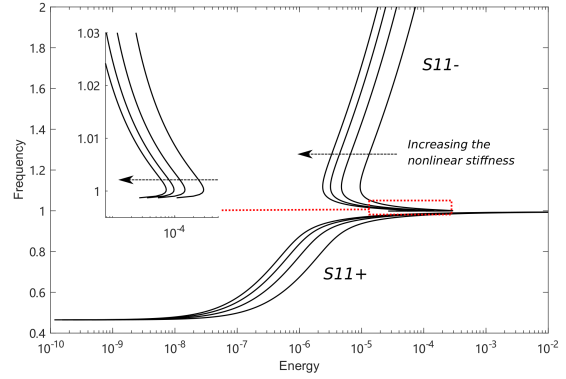


Fig. 2. Frequency-energy plot for the different cubic stiffnesses K , $\epsilon = 0.01$, $\delta = -0.436$, (K values are selected as 1000, 2000, 3000 and 4000 respectively, following the direction of the arrow). Zoomed insert represents detailed curve trends in the region in the red frame, near the frequency 1

The conservative energy of the system follows:

$$E(\Omega) = \frac{1}{2}\epsilon\delta(V - Y)^2 + \frac{1}{4}\epsilon K(V - Y)^4 + \frac{1}{2}Y^2 \quad (7)$$

Combining the expression of Y and V , Eqn. (7) leads to Fig. 2 and 3 under the influence of the different parameters. The curve is divided into two branches by the forbidden zone [5], where the ratio of two real positive amplitudes becomes negative. The S11- exists only the upper branch ($\Omega > 1$) and the S11+ exists for $\Omega < \sqrt{\frac{1}{1+\epsilon}}$. The saddle points on the S11- can be calculated by deriving the conservative system energy with respect to Ω , $E'(\Omega) = 0$. The two real roots correspond to the frequency of Ω_1 and Ω_2 of saddle point 1 and point 2, and their energy levels $E_1 = E(\Omega_1)$, $E_2 = E(\Omega_2)$ (see Fig. 7). The unstable branch in energy range $[E_1, E_2]$ can be explained based on the LPT concept. The energy interval $[E_1, E_2]$ plays an essential role in TET mechanism on the S11- branch. When the system satisfies the critical condition [27], the slow flow produces two stable stationary points and one unstable one on the S11- branch of the two-torus process, where the phase difference between the variables x and y is equal to π , out-phase 1:1 resonance. In this condition, the LPT coalesces with a homoclinic orbit. By designing the proper parameter, the system has the most conservative energy and highly intensive energy exchange.

Fig. 2 shows the influence of increasing K values on the energy level of saddle point 2 and leads to E_2 become higher. A lower K can adapt to the higher energy level for efficient TET. An interesting phenomenon is that the ratio of energy interval E_1/E_2 is almost constant in Fig. 2, which shows the parallel translation of the upper S11- branch on the logarithmic axis with the variation of K .

Increasing negative stiffness results in extending the distance between the saddle points $[E_1, E_2]$ in Fig. 3. It improves the performance of energy transfer for relatively high energy

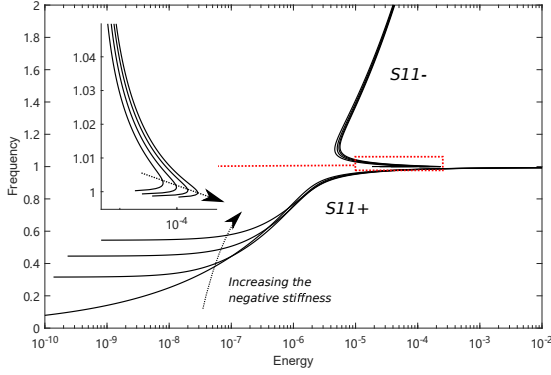


Fig. 3. Frequency-energy plot for the different linear negative stiffnesses δ ($\varepsilon = 0.01$, $K = 1754$, δ value is selected as 0, -0.2, -0.4 and -0.6 respectively, following the direction of the arrow). Zoomed plot represents detailed curve trends in the region marked in red frame, near the frequency 1

input. Hence, K and δ can be tailored to absorb certain input energies.

3 Asymptotic analysis for non-conservative systems

The existence of damping causes the initial high input energy to be dissipated over time. The various stages alter according to a residual energy level [9]. The negative stiffness helps the bistable NES maintain a capacity for passive targeted energy transfer at low energy level [28].

With the existence of harmonic excitation (constant energy input), the different stages can be maintained. In cubic case, the periodic response is activated until the threshold force of SMR is achieved. If the excitation continues to increase, the SMR disappears and returns to be a periodic response again. In the bistable case, the response regimes are divided into four stages according to [19]: (a) intra-well oscillation; (b) chaotic inter-well oscillation; (c) strongly modulated response; (d) stable periodic response.

To describe the above regimes precisely, the new variables $v = x + \varepsilon y$, $w = x - y$ are substituted into Eqn. (3):

$$\begin{aligned} \ddot{v} + \varepsilon \lambda_1 \frac{\dot{v} + \varepsilon \dot{w}}{1 + \varepsilon} + \frac{v + \varepsilon w}{1 + \varepsilon} &= \varepsilon F \cos \Omega t \\ \ddot{w} + \varepsilon \lambda_1 \frac{\dot{v} + \varepsilon \dot{w}}{1 + \varepsilon} + \frac{v + \varepsilon w}{1 + \varepsilon} + \lambda_2 (1 + \varepsilon) \dot{w} & \\ + K(1 + \varepsilon) w^3 + \delta(1 + \varepsilon) w &= \varepsilon F \cos \Omega t \end{aligned} \quad (8)$$

Under the assumption of 1:1 resonance, the LO and NES execute time-periodic oscillations with an identical frequency of Ω . The Manevitch complex variables $\phi_1 e^{i\Omega t} = \dot{v} + i\Omega v$, $\phi_2 e^{i\Omega t} = \dot{w} + i\Omega w$ are introduced into Eqn. (8). Only terms containing the $e^{i\Omega t}$ are left.

$$\begin{aligned} \dot{\phi}_1 + \frac{i\Omega}{2} \phi_1 + \frac{\varepsilon \lambda_1 (\phi_1 + \varepsilon \phi_2)}{2(1 + \varepsilon)} - \frac{i(\phi_1 + \varepsilon \phi_2)}{2\Omega(1 + \varepsilon)} - \frac{\varepsilon F}{2} &= 0 \\ \dot{\phi}_2 + \frac{i\Omega}{2} \phi_2 + \frac{\varepsilon \lambda_1 (\phi_1 + \varepsilon \phi_2)}{2(1 + \varepsilon)} - \frac{i(\phi_1 + \varepsilon \phi_2)}{2\Omega(1 + \varepsilon)} + \frac{\lambda_2 (1 + \varepsilon) \phi_2}{2} & \\ - \frac{3iK(1 + \varepsilon) \phi_2^2 \bar{\phi}_2}{8\Omega^3} - \frac{\varepsilon F}{2} - \frac{i\phi_2 \delta(1 + \varepsilon)}{2\Omega} &= 0 \end{aligned} \quad (9)$$

The periodic solution of Eqn. (9) can be calculated under the assumption that the derivative is zero. By extracting the expression of periodic solution ϕ_{10} substituted by variables ϕ_{20} and then introducing it into the second equation of (9), a more convenient expression can describe the system, where $\Omega = 1$.

$$K^2 \alpha_3 Z_{20}^3 + K \alpha_2 Z_{20}^2 + \alpha_1 Z_{20} + \alpha_0 = 0, \quad Z_{20} = |\phi_{20}|^2 \quad (10)$$

where

$$\begin{aligned} \alpha_0 &= -\frac{1}{4} \frac{(\varepsilon^2 \lambda_1^2 + 1) F^2 (1 + \varepsilon)^2}{\lambda_1^2 + 1} \\ \alpha_1 &= \frac{1}{4} \frac{(\lambda_1^2 \lambda_2^2 + \lambda_1^2 + 2\lambda_1 \lambda_2 + \lambda_2^2) (1 + \varepsilon)^2}{\lambda_1^2 + 1}, \quad (11) \\ \alpha_2 &= -\frac{3}{8} \frac{(1 + \varepsilon)^2 \lambda_1^2}{\lambda_1^2 + 1}, \quad \alpha_3 = \frac{9}{64} (1 + \varepsilon)^2 \end{aligned}$$

To obtain the analytical threshold value for SMR, a perturbation method and the multiple scales method are used with respect to the small parameter $\varepsilon \approx 1\%$

$$\begin{aligned} \phi_i &= \phi_i(\tau_0, \tau_1, \dots), \quad \frac{d}{dt} = \frac{\partial}{\partial \tau_0} + \varepsilon \frac{\partial}{\partial \tau_1} + \dots \\ \tau_k &= \varepsilon^k \tau, \quad k = 0, 1, \dots \end{aligned} \quad (12)$$

Substituting Eqn. (12) into Eqn. (9), terms that contain a coefficient of ε^0 give:

$$\begin{aligned} \frac{d}{d\tau_0} \phi_1 &= 0 \\ \frac{d}{d\tau_0} \phi_2 + \frac{1}{2} i (\phi_2 - \phi_1) + \frac{1}{2} \phi_2 \lambda_2 - \frac{3}{8} i K \phi_2^2 \bar{\phi}_2 - \frac{1}{2} i \delta \phi_2 &= 0 \end{aligned} \quad (13)$$

Order ε^1 (where σ is a detuning parameter defined as $\Omega = 1 + \varepsilon \sigma$):

$$\begin{aligned} \frac{d}{d\tau_1} \phi_1 + \frac{1}{2} \lambda_1 \phi_1 + \frac{1}{2} i (\phi_1 - \phi_2) + i \sigma \phi_1 - \frac{1}{2} F &= 0 \\ \frac{d}{d\tau_1} \phi_2 + \frac{1}{2} \lambda_1 \phi_1 + \frac{1}{2} \phi_2 \lambda_2 + \frac{1}{2} i \sigma (\phi_1 + \phi_2) & \\ + \frac{1}{2} i (\phi_1 - \phi_2) - \frac{3}{8} i K (1 - 3\sigma) \phi_2^2 \bar{\phi}_2 - \frac{1}{2} F + \frac{1}{2} i \delta (\sigma - 1) \phi_2 &= 0 \end{aligned} \quad (14)$$

4 Cubic NES response regimes

The cubic case is defined by setting $\delta = 0$. To study the stable amplitude of LO and NES, the new variables $\phi_1(\tau_1) = N_1 e^{i\theta_1}$, $\phi_2(\tau_1) = N_2 e^{i\theta_2}$ are introduced into Eqn. (13) and the derivative term is set to zero. It gives an expression that describes the topological structure of the SIM of a cubic system:

$$\begin{aligned} Z_1 &= \lambda_2^2 Z_2 + Z_2 - \frac{3K}{2} Z_2^2 + \frac{9K^2}{16} Z_2^3 \\ Z_1 &= N_1^2, \quad Z_2 = N_2^2 \end{aligned} \quad (15)$$

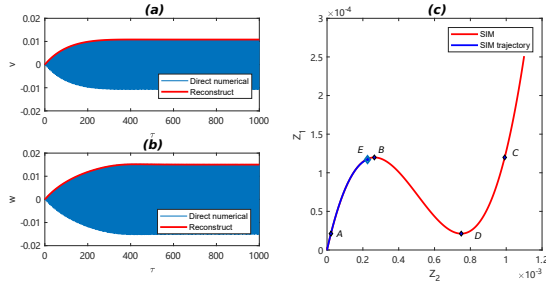


Fig. 4. Case a: Cubic NES response under low energy input ($G=0.022\text{mm}$). Subplots (a) and (b) represent the time-displacement response, the red curve is the reconstructed envelope amplitude (c) reconstructed trajectory projection (blue) in SIM structure (red)

The SIM is shown in the red line in the right side of Fig. 4. It represents the intrinsic property of the system and its independence with respect to external excitation. The red line envelope in the left figure is the reconstructed w and v originating from Eqn. (9).

In the cubic NES, the SMR is an essential characteristic. The detailed description of the SMR and its stability has been investigated in [29]. The SMR should satisfy some conditions to be triggered. The force threshold interval has been indicated in [11, 30]. Since the excitation is at the same frequency as the natural frequency of the primary system and the mass ratio is sufficiently small ($\epsilon \ll 1$), the effect of the detuning parameter and the mass ratio is beyond the scope of this work.

According to [11], the excitation thresholds G_{1c} are given by:

$$G_{1c} = \frac{\epsilon N_{2,i} \left(9\lambda_1 K^2 N_{2,i}^4 - 24\lambda_1 K N_{2,i}^2 + 16(\lambda_1 + \lambda_2 + \lambda_1 \lambda_2^2) \right)}{4\sqrt{9K^2 N_{2,i}^4 - 24KN_{2,i}^2 + 16 + 16\lambda_2^2}} \quad (16)$$

$$Z_{2,i} = N_{2,i}^2 = \frac{4}{9} \frac{2 \mp \sqrt{-3\lambda_2^2 + 1}}{K}, i = 1, 2 \quad (17)$$

The $Z_{2,1}$ and $Z_{2,2}$ are the values of Z_2 at saddle point B and D in Fig. 6. The values of the parameters such as $\epsilon = 0.01, \lambda_1 = 1.67, \lambda_2 = 0.167, K = 1754$ are fixed in the cubic case. When the harmonic excitation is too small to activate efficient energy pumping, the response of LO and NES appears to be a periodic response with constant amplitude as in Fig. 4. There is only an ordinary fixed point on the phase portrait of the SIM. The trajectory of amplitude in the time domain rises along the SIM over time, and its final point E is located on left the SIM stable branch. With the increasing harmonic force, the final stable amplitude point E , is closer to the jumping point, B , before 'jump'.

When the excitation exceeds the critical value of excitation G_{1c} , a saddle node bifurcation occurs. The existence of

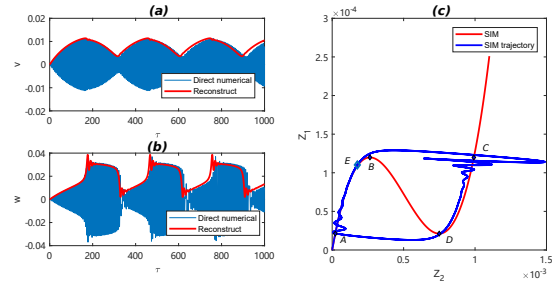


Fig. 5. Case b: Cubic NES response under mid energy input ($G=0.028\text{mm}$). Subplots (a) and (b) represent the time-displacement response, the red curve is the reconstructed envelope amplitude (c) reconstructed trajectory projection (blue) in SIM structure (red)

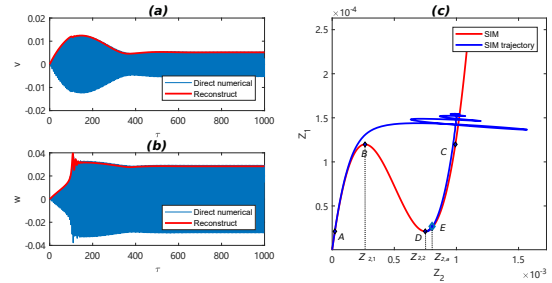


Fig. 6. Case c: Cubic NES response under high critical energy input ($G=0.038\text{mm}$), where SMR just disappears. Subplots (a) and (b) represent the time-displacement response, red curve is the reconstructed envelope amplitude (c) reconstructed trajectory projection (blue) in SIM structure (red)

folded singularities results in the relaxation-type oscillation phenomenon. The trajectory of the system in Fig. 5 has a 'jump' motion between the two stable branches. A complete 'jump' cycle consists of a trajectory $A - B - C - D - A$ on the SIM branch. The displacements on the stable branch for the stage $A - B$ and $C - D$ coincide closely with the backbone of the SIM, and the 'jump' motion only appears in the $B - C$ and $D - A$ stages. Once the trajectory returns to point A , a new SMR cycle starts.

If the excitation continues to grow and surpasses the upper boundary G_{2c} of SMR interval, the SMR disappears and a regular fixed point occurs on the phase portrait of the SIM. The regular fixed point corresponds to a periodic response. The trajectory of the system in Fig. 6 arrives at the final stable point, E , located on the SIM stable branch, close to the 'jump' point D of the right branch.

4.1 Influence of damping and stiffness on conservative energy

To describe the conservative energy in a non-conservative system, the critical energy level before the SMR occurs and after it disappears are presented in Fig. 7. The energy level when SMR appears (blue line) almost coincides with the saddle point (ω_1, E_1), and the energy level when SMR disappears (red line) is close to the endpoints of the upper branch energy level E_1 . The conservative energy level

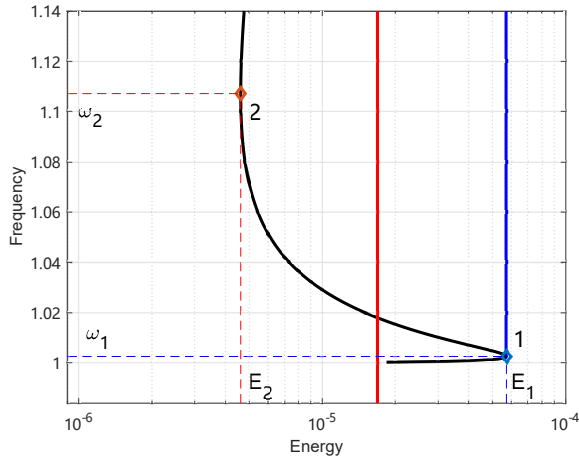


Fig. 7. Energy range of intensive energy exchange in cubic NES case ($\delta = 0, \lambda_1 = 1.67, \lambda_2 = 0.167, K = 1754$). The black curve is the backbone of the frequency-energy relation, the blue line is the threshold energy for SMR to appear, and the red line is the threshold energy for SMR to disappear

when SMR disappears (red line in Fig. 7) is much lower than that when SMR occurs. This shows that energy has been dissipated through the SMR mechanism even if the input energy continues to increase from E_1 to E_2 .

The influence of the damping parameter on the conservative energy in the systems is analysed in Fig. 8. The red curve is the SMR interval, which is an unstable region. Its stability is confirmed by Floquet theory. Under the various damping parameters, the level of conservative energy necessary to trigger the SMR is almost constant, about $5.7 \times 10^{-5} J$. For the energy level for SMR to disappear, the λ_2 have a more significant impact on the determination of the critical value, the curve groups with the same λ_2 result in similar local minima.

To explain why the trigger conservative energy level is the same under different damping conditions, a 'weak damping' assumption is proposed, where λ_2 tends to be zeros. On the SIM, the ratio of the amplitude of LO and NES at the jumping point B is 1.5. The existence of the small parameter ε results in the conservative energy is mainly governed the amplitude of LO, so it becomes $E \approx \frac{1}{2} Y^2 = \frac{8}{81K}$. The trigger energy level is determined mainly by the nonlinear stiffness K .

In order to verify the correctness of this approximation, the critical energy levels calculated using the different methods are compared in Tab. 1. The first column is the energy level at the saddle point (E_1, ω_1). The stable amplitude of LO and NES before the SMR appears is calculated using the numerical method that forms the second column. The third column is the predicted trigger energy level. In the same nonlinear stiffness condition, the three critical trigger energy levels are practically the same, which confirms that this approximation $\frac{8}{81K}$ is correct and is determined mainly by K .

It can be clearly observed that the conservative energy

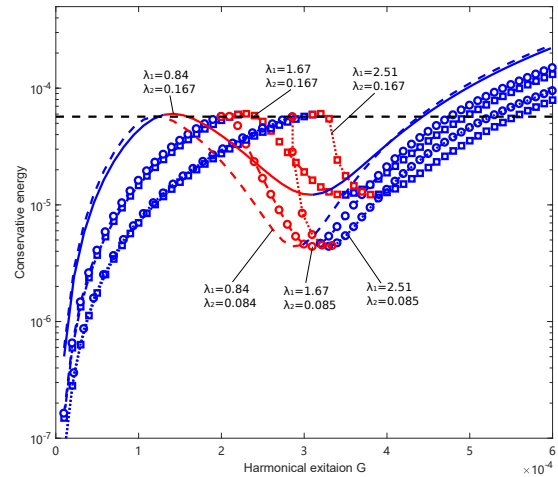


Fig. 8. Variety of the conservative energy in the different damping systems ($\varepsilon = 0.01, K = 1754$). The blue curve is calculated by stable solution, the red curve is calculated by unstable amplitude, the black dashed line represents the energy level $5.7 \times 10^{-5} J$

Table 1. The comparison of SMR occurs energy level in different nonlinear stiffnesses K cases

K	Energy level in saddle point	Calculated trigger energy level	$\frac{8}{81K}$
2613	3.82e-5	3.81e-5	3.83e-5
1754	5.73e-5	5.71e-5	5.74e-5
871	1.15e-4	1.15e-4	1.15e-4

when SMR starts to occur is the same as the energy level of a saddle point in Fig. 9, which shows the frequency-energy relationship for different nonlinear stiffnesses. This means that the conservative energy threshold at the saddle point can be considered as an indication that SMR occurs. It is difficult to obtain an analytical expression for the energy level at the saddle point based on the previous discussion. However, the simulations of different damping parameters and different nonlinear stiffnesses in Fig. 8 and 9 reveal that the SMR always happens when the system's conservative energy achieves its critical value. This critical energy level is determined mainly by the nonlinear stiffness K without considering the damping condition. This can help us predict the occurrences of SMR without having precise knowledge of the damping parameters.

4.2 Efficiency of cubic NES

To better understand the efficiency with which the input energy is absorbed during the different stages, the energy

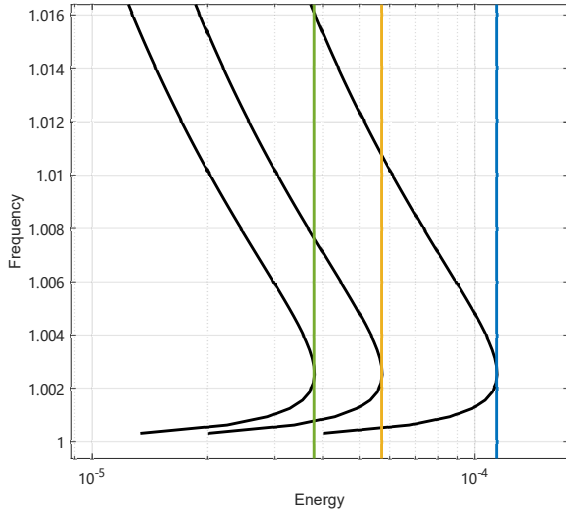


Fig. 9. Critical energy level triggering SMR for different nonlinear stiffnesses K on the frequency-energy plot (blue: $K = 2613$; yellow: $K = 1754$; green: $K = 871$). The stiffnesses K of black backbones from right to left are same with condition corresponding to tangent colourful lines

dissipation ratio is defined in the time interval $[\tau_0, \tau]$ as:

$$\begin{aligned} E_{LO}(\tau) &= \int_{\tau_0}^{\tau} \varepsilon \lambda_1 \dot{x}^2 d\tau \\ E_{NES}(\tau) &= \int_{\tau_0}^{\tau} \varepsilon \lambda_2 (\dot{x} - \dot{y})^2 d\tau \\ r_{NES} &= \frac{E_{NES}}{E_{NES} + E_{LO}} 100\% \end{aligned} \quad (18)$$

Figure. 10 shows that the 3 response stages are divided by the analytical SMR interval $[G_{1c}, G_{2c}]$. When the input energy ($G < G_{1c}$) is too weak to activate the SMR, the mean amplitude (A_e) and maximum amplitude (A_m) coincide and increase linearly with the force. Once the harmonic force is strong enough to activate the SMR, the difference between A_m and A_e reveals that the amplitude of the NES is no longer stable. In comparison with the previous stage, the NES possesses more energy. This is referred to as the TET mechanism. Even though the external excitation is increasing, the maximum amplitude of LO remains almost constant. When the force exceeds the G_{2c} threshold value, the curves of A_m and A_e coalesce again and become stable. With a slight increase in force, the system achieves its maximum efficiency point and the amplitude of LO is a local minimum, which means that the full potential of absorbing energy has been explored.

Considering $N_{2,2}$ as the amplitude of NES at the transition point D , the optimal stiffness can be calculated by solving Eqn. (10) when a harmonic force $F = G/\varepsilon$ is imposed on the system:

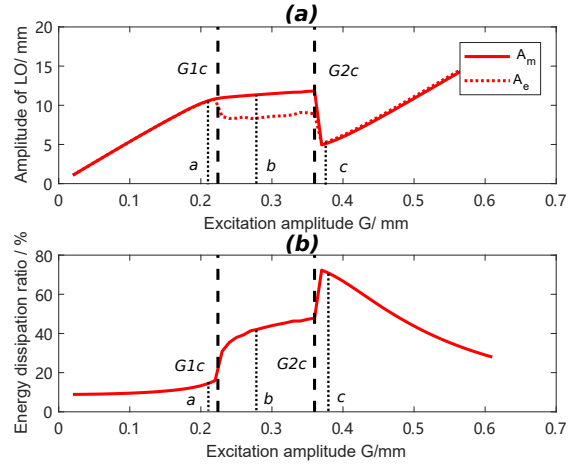


Fig. 10. Efficiency of cubic NES (a) the maximum amplitude (A_m) and mean amplitude (A_e) of LO ($\varepsilon = 0.01, \lambda_1 = 1.67, \lambda_2 = 0.167, K = 1754$), (b) Energy dissipation ratio of NES. Dotted lines a, b and c in figures represent condition in Fig. 4, 5 and 6

$$\begin{aligned} K &= -\frac{4}{729} \frac{1}{\alpha_0} \left(16(-3\lambda_2^2 + 1)^{3/2} \alpha_3 - 108\lambda_2^2 \alpha_2 \right. \\ &\quad - 288\lambda_2^2 \alpha_3 + 81\sqrt{-3\lambda_2^2 + 1} \alpha_1 \\ &\quad + 144\alpha_2 \sqrt{-3\lambda_2^2 + 1} + 192\sqrt{-3\lambda_2^2 + 1} \alpha_3 \\ &\quad \left. + 162\alpha_1 + 180\alpha_2 + 224\alpha_3 \right) \end{aligned} \quad (19)$$

The amplitudes of LO under different nonlinear stiffnesses and various harmonic forces are presented in Fig. 11 to check the accuracy of the predictions. The various nonlinear stiffnesses are tested under a certain excitation to find an optimal nonlinear stiffness K .

The thick red line corresponds to the numerical optimal stiffness curve. It represents the projection of the minimum amplitude that LO can have for a certain excitation in the $K - G$ plane. The thin red and blue lines are the maximum and mean amplitudes respectively. The SMR occurs in the region, where these lines do not coincide. The dotted and dashed thick blue lines represent the analytical optimal stiffness with and without correction coefficient ξ respectively.

An obvious trend is observed: a larger imposed force (input energy) leads to a smaller designed nonlinear stiffness. It confirms the conclusion obtained by a frequency-energy analysis in a conservative system. There is a distance between the real and predicted curves. The distance can be interpreted as the errors between the analytical arrival point D and real arrival point E in Fig. 6.

Ideally, once the SMR vanishes, the final stable solution should be located at foleded point D . In fact, the simulation demonstrates that the real final stable point does not coincide with point D , but is slightly higher on the SIM. The theoretical amplitude threshold Z_{22} may be smaller than the simulated value Z_{2a} , leading to errors between the analytical and numerical $K - G$ curves.

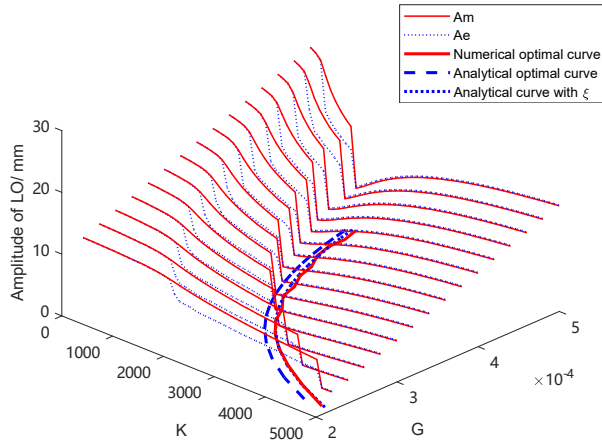


Fig. 11. Distribution of the LO amplitude with the variation of harmonic forces G and nonlinear stiffnesses K ($\lambda_1 = 1.67, \lambda_2 = 0.167, \varepsilon = 0.01$)

Considering the correction coefficient $\xi = 1.07$ to describe the distance between the analytical arrival point $Z_{2,2}$ and simulated arrival point $Z_{2,a} = \xi Z_{2,2}$, ξ is introduced into Eqn. (16) to resolve the K . The corrected predicted curve (thick blue dotted line in Fig. 11) almost coincides with the real optimal $K - G$ curve.

The correction coefficient ξ helps improve the accuracy in the prediction of the optimal stiffness. If the nonlinear stiffness of the system exceeds the optimal value, then the response of the system will remain stable. For example, the nonlinear stiffness must be tuned to 1500 in order to minimise the amplitude of LO (5.3 mm) under excitation ($G = 0.4$ mm) (Fig. 11). When the K value is extended to 3400, the LO possesses a minimum stable amplitude of 10.2 mm, which is smaller than the mean amplitude of the LO during SMR (10.26 mm). Thus, in the K -value range [1500, 3400], cubic NES can achieve a better absorption performance than SMR. A vast range of K can be chosen. When the system faces uncertainties in the K value, it shows a strong robustness. The absorption efficiency can be maintained at a relatively high level if the stiffness is slightly larger than the optimal value. Even if the value of K is lower than the optimal value, the response is SMR, which is still considered to be highly efficient.

When it reaches its ideal maximum efficiency point D , the system has a periodic response and constant amplitude. The response of w can be expressed as $w = N_{2,2} \cos(\tau + \delta_1)$ approximately. In the whole period (τ to $\tau + 2\pi$), the energy dissipated by NES can be rewritten as:

$$\int_{\tau}^{\tau+2\pi} \varepsilon \lambda_2 \dot{w}^2 d\tau = \int_{\tau}^{\tau+2\pi} \varepsilon \lambda_2 \left(-N_{2,2}^2 \sin(\tau + \delta_1) \right)^2 d\tau \quad (20)$$

$$= \varepsilon \lambda_2 N_{2,2}^2 \pi$$

As for the energy dissipated by the LO, the velocity \dot{x} , the x can be expressed as $x = v - \varepsilon y$, where the ε is an

extremely small parameter and leads to $x \approx v$. So, at the maximum efficiency point, x is $N_{1,2} \cos(\tau + \delta_2)$. Similarly to Eqn. (20), the energy dissipated by the LO in the whole period is $\varepsilon \lambda_1 N_{1,2}^2 \pi$. So the maximum efficiency point during one period is

$$r_{NES} = \frac{\lambda_2 N_{2,2}^2}{\lambda_1 N_{1,2}^2 + \lambda_2 N_{2,2}^2} \quad (21)$$

According to the Eqn. (17), from a theoretical point of view, the above equation is finally turned into the following form:

$$r_{NES} = -\frac{9\lambda_2}{-6\lambda_1\lambda_2 + 2\sqrt{-3\lambda_2^2 + 1\lambda_1 - 2\lambda_1 - 9\lambda_2}} \quad (22)$$

This equation shows that the ceiling of maximum theoretical efficiency is determined only by the damping λ_1 and λ_2 . Subplot (a) of Fig. 12 depicts its maximum theoretical efficiency values for different damping conditions. In fact, the ideal amplitude of NES and LO for the instant the SMR disappears shows some differences with simulation, which leads to the error between the analytical maximum efficiency value and the simulated value.

The distribution of parameters ξ in the λ_1, λ_2 plane can be used to correct predicted maximum efficiency, shown in subplot (b) of Fig. 12. The analytical value $Z_{2,2}$ produces greater errors than the simulated value $Z_{2,a}$ in the lower λ_1, λ_2 values. In contrast, the analytical value $Z_{2,2}$ can better describe the arrival point $Z_{2,a}$ for a relatively high damping parameter. So the maximum efficiency value when considering the correction coefficient ξ can be rewritten as:

$$r_{NES} = 9\lambda_2 / ((4\xi^2 - 6\xi) \sqrt{-3\lambda_2 + 1\lambda_1} + (-3\xi^2 + 9) \lambda_1 \lambda_2^2 + \lambda_1 (5\xi^2 - 12\xi) + 9(\lambda_1 + \lambda_2)) \quad (23)$$

The distribution of maximum efficiency based on Eqn. (23) is illustrated in subplot (c) of Fig. 12. It demonstrates that for certain fixed λ_1 , an optimal damping value λ_2 exists to promote the energy-absorbing performance. Reducing the damping on the preliminary structure λ_1 can enhance the maximum absorbing efficiency value.

The three different damping conditions, labelled in subplot (c) of Fig. 12 as condition 1, 2 and 3, are used to verify the analytical prediction of maximum efficiency. The predicted values for condition 1, 2 and 3, are obtained directly by Eqn. (23) with different correction coefficients $\xi = 1.12, 1.06, 1.13$ from subplot (b), are 77%, 71% and 53% respectively. The direct calculations of maximum efficiency of 76%, 68% and 52%, which are very close to the predicted values. A simpler way to estimate maximum efficiency value has been found.

To verify that the maximum absorbing efficiency values are independent of the optimal nonlinear stiffness design,

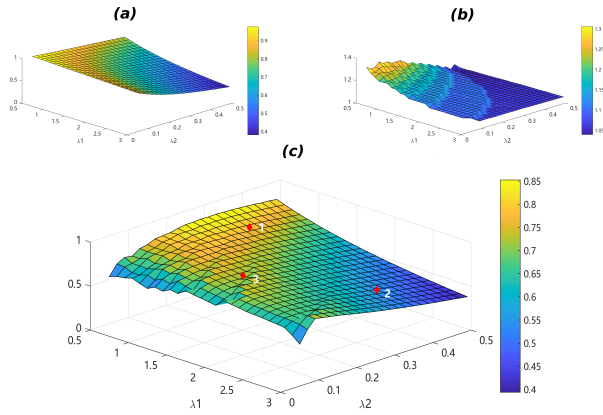


Fig. 12. Maximum efficiency values and correction coefficient ξ in the function of λ_1 and λ_2 in case $K = 1754$ and $\varepsilon = 0.01$. (a) ideal maximum efficiency estimated by Eqn. (22) (b) correction coefficient ξ distribution (c) maximum efficiency values with ξ corrected by Eqn. (23), point 1, 2 and 3 are the 3 conditions to be verified.

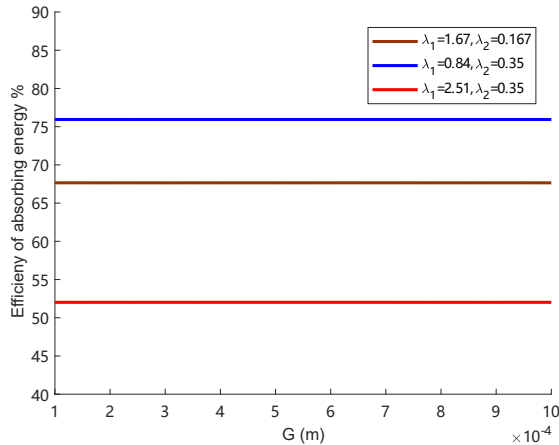


Fig. 13. Maximum energy dissipation ratio that a best tuned K system for certain excitation G can achieve under the different damping parameters conditions

various simulations are performed in the different damping environments, as shown in Fig. 13. Each point on the excitation-efficiency line represents the maximum efficiency value achievable for the corresponding optimal cubic stiffness design with correction coefficients from Eqn. (19). For every variation in excitation from 0.01mm to 0.1mm, the optimal stiffness design changes according to Fig. 11 but the maximum efficiency value is almost constant. This phenomenon indicates that the maximum ability to absorb energy is independent of the stiffness design. The stiffness design can only adopt a certain excitation input and its maximum efficiency is determined by the damping conditions.

According to Eqn. (22), the nonlinear stiffness K and mass ratio ε do not influence the limit of maximum efficiency. However, because the prerequisite of the above result is the existence of SMR, the restrict of $\lambda_2 < 1/\sqrt{3}$, and not too high a mass ratio ε is still necessary [31].

5 Bistable NES response regimes

If δ is negative, Eqn. (8) can describe the motion of bistable NES. The NES has two equilibrium points, one on either side of the cubic NES original coordinate, with the presentation of negative linear stiffness.

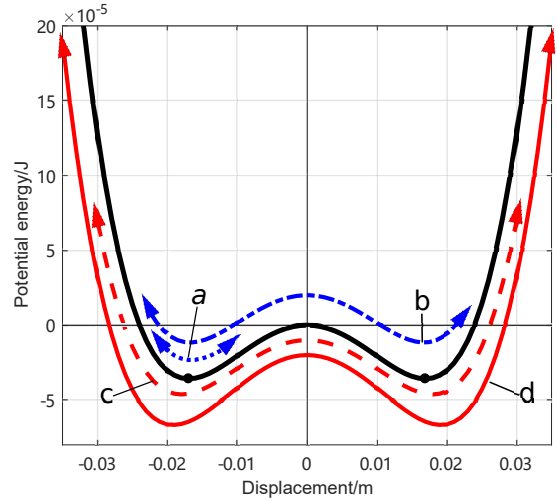


Fig. 14. Potential function of the unperturbed system:(a) an intra-well oscillation; (b) chaotic inter-well oscillation; (c) strongly modulated response; (d) stable periodic response.

In our study, the second equation of bistable NES system: $\ddot{w} + \lambda_2 \dot{w} + Kw^3 + \delta w = \ddot{x}$ can be expressed in following equation with the definition $\lambda_2 = \varepsilon \hat{\lambda}_2, \ddot{x} = \varepsilon \hat{x}$. It is necessary to consider the acceleration term and damping term as small perturbations to the Hamiltonian system.

$$\begin{cases} \dot{u}_1 = u_2 \\ \dot{u}_2 = -\delta u_1 - Ku_1^3 + \varepsilon (\hat{x} - \hat{\lambda}_2 u_2) \end{cases} \quad (24)$$

The Hamiltonian system without perturbation and its potential function can be written as:

$$\begin{aligned} H(u_1, u_2) &= \frac{u_2^2}{2} + \delta \frac{u_1^2}{2} + K \frac{u_1^4}{4} \\ U(u_1) &= \delta \frac{u_1^2}{2} + K \frac{u_1^4}{4} \end{aligned} \quad (25)$$

In the bistable case, the system is characterized by a double-well potential energy surface, which is presented in Fig. 14. Three equilibrium points exist: $(u_1, u_2) = (0, 0)$ and $(u_1, u_2) = (\pm\sqrt{-\delta/K}, 0)$. The K governs the span of two wells $2\sqrt{-\delta/K}$ (the distance between two equilibria) and the depth of well $\Delta w = -\delta^2/4K$. When the energy of the NES is lower than Δw , it will be trapped in one of the two wells. So K and δ determine the lower boundary of energy above which bistable NES performs a cross-well oscillation. In contrast to the influence of K , larger values of δ

increase the span and depth of the potential well. According to the location of potential energy surface of bistable NES, its response regimes can be classified in four following stages. The parameters of this bistable NES case are fixed as: $\varepsilon = 0.01, \lambda_1 = 1.67, \lambda_2 = 0.167, K = 1754, \delta = -0.44$.

(a) Intra-well oscillation

When the energy is below the critical value, the potential energy is in one of the wells as in case *a* in Fig. 14. Since the nonlinear stiffness is far larger than that of cubic NES near the stable equilibrium, nonlinear beating can be produced with relatively high efficiency for low energy input.

(b) Chaotic inter-well oscillation

Once the input energy increases, the trajectory will pass the pseudo-separatrix and oscillate between two wells, therefore, chaos occurs. If the excitation continues to increase, the SMR appears and mixes with the chaotic oscillation. According to Fig. 15, the trajectory will still cross the wells but will oscillate above the pseudo-separatrix half of the time. The energy pumping will occupy more and more time. The chaos almost disappears until the excitation exceeds the threshold value G_{2c} . On the other hand, the subharmonic 1:3 phenomenon, which leads to a relatively low energy absorbing ratio, has been confirmed in [32].

(c) Strongly modulated response

When NES amplitude continues to grow, the nonlinear stiffness has a larger effect on the response behaviour. The SMR response replaces the chaotic motion in the time domain. In Fig. 16, the trajectory of the SMR is more focused in a certain Hamiltonian energy height range. Few trajectories pass the well. Returning to the well is also necessary to restart a new turn of SMR.

(d) Stable response

The system reaches a stable state, and the SMR disappears. In Fig. 16, the trajectory becomes a narrow closed cycle, which means it has a constant amplitude and reaches a stable response. The efficiency of the NES reaches its maximum value between the transition from the SMR stage to the stable response stage.

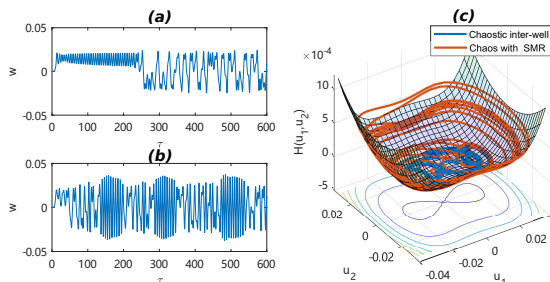


Fig. 15. Time-displacement response of NES and its phase trajectory on Hamiltonian surface: (a) chaotic inter-well oscillation with $G = 0.1mm$ (b) chaos incomplete SMR response with $G = 0.25mm$ (c) projection of phase trajectory on the H surface

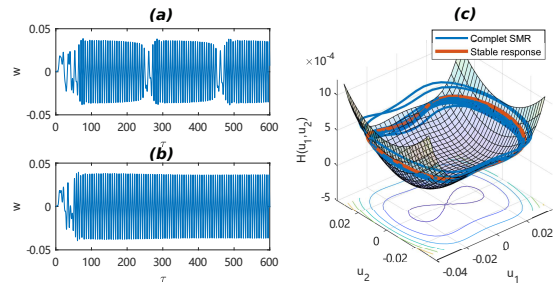


Fig. 16. Time-displacement response of NES and its phase trajectory on Hamiltonian surface: (a) Complete SMR response with $G = 0.4mm$ (b) stable response with $G = 0.5mm$ (c) projection of phase trajectory on the H surface

5.1 Damping parameter boundary for chaos

Chaos in bistable NES is a complex behaviour. To better predict the boundary of chaos response, a Melnikov analytical method is applied in [28] to identify the chaotic behaviours. The Melnikov method is one of the few effective ways to analyse homoclinic bifurcation and detect the occurrence of chaos. The Melnikov method describes the distance between stable and unstable manifolds of the perturbed system and can estimate the occurrence of global bifurcation in the parameter space [18]. Before applying the Melnikov method, the system is considered in a special form:

$$\dot{z} = f(z) + \varepsilon g(z, t); \quad z = \begin{Bmatrix} u_1 \\ u_2 \end{Bmatrix} \in R^2 \quad (26)$$

where $f(z)$ is a Hamiltonian vector and $\varepsilon g(z, t)$ is a smaller perturbation, which does not require to be Hamiltonian. To analyse its stability near the equilibrium point, the Jacobian matrix of the unperturbed system is expressed:

$$J = \begin{bmatrix} 0 & 1 \\ -\delta - 3Ku_1^2 & 0 \end{bmatrix} \quad (27)$$

Its eigenvalues are $\lambda = \pm \sqrt{-\delta - 3Ku_1^2}$. One of eigenvalues $\lambda_{1,2} = \pm \sqrt{-\delta}$ has a pure positive real part near the fix point $(0, 0)$, so this equilibrium points is a saddle. For the other two fixed point $(\pm \sqrt{-\delta/K}, 0)$, the eigenvalues are $\lambda_{1,2} = \pm \sqrt{2\delta}$. Because parameter δ is defined as a negative value, the eigenvalues are purely imaginary and these two fixed points are centres. The unperturbed homoclinic orbit that connects the saddle points is given by:

$$\begin{cases} q_+^0(\tau) = (R \cdot \text{sech}(S\tau), -RS \cdot \text{sech}(S\tau) \tanh(S\tau)) \\ q_-^0(\tau) = -q_+^0(\tau) \end{cases} \quad (28)$$

where $S = \pm \sqrt{-\delta}$ and $R = \sqrt{-2\delta/K}$. The homoclinic bifurcation describes the transverse insertion of stable and

unstable manifolds of a saddle fixed point. It is an obvious symbol of chaotic behaviours. This hyperbolic orbit distinguishes whether the phase diagram of the system is intra-well oscillation or inter-well oscillation. When the potential energy arrives to its local maximum $u_1 = 0$, the centre of the phase trajectory shifts from a centre fixed point to a saddle equilibrium, and chaos will occur. This transition is a result of the change of excitation or the inner system parameter. The homoclinic orbit breaks and may cross manifolds when the perturbed terms are considered. For simplicity, the Melnikov function can be expressed:

$$M(\tau_0) = \sqrt{\frac{2}{K}} \frac{N_1 \pi \Omega^3}{\varepsilon} \sin(\Omega \tau_0 + \phi) \operatorname{sech}\left(\frac{\pi \Omega}{2\sqrt{-\delta}}\right) \pm \frac{4\delta\sqrt{-\delta}}{3K} \frac{\lambda_2}{\varepsilon} \quad (29)$$

The condition for traversing the intersection of stable and unstable manifolds is satisfied when $M(\tau_0) = 0$.

$$\left| \sqrt{\frac{2}{K}} \frac{N_1 \pi \Omega^3}{\varepsilon} \operatorname{sech}\left(\frac{\pi \Omega}{2\sqrt{-\delta}}\right) \right| > \left| \frac{4\delta\sqrt{-\delta}}{3K} \frac{\lambda_2}{\varepsilon} \right| \quad (30)$$

$$\lambda_2(1) < \frac{3\sqrt{2KN_1}\pi\Omega^3}{4\delta\sqrt{-\delta}} \operatorname{sech}\left(\frac{\pi\Omega}{2\sqrt{-\delta}}\right) \quad (31)$$

$$\lambda_2(2) > -\frac{3\sqrt{2KN_1}\pi\Omega^3}{4\delta\sqrt{-\delta}} \operatorname{sech}\left(\frac{\pi\Omega}{2\sqrt{-\delta}}\right)$$

In other words, with the above equation, the interval of damping parameter λ_2 required to avoid the occurrence of chaos at the critical amplitude N_1 can be determined. For a designed amplitude of LO of $N_1 = 3mm$, the threshold curves are shown in Fig. 17. The critical value of damping λ_2 equals to 0.266, where the critical excitation force $G = 0.091mm$ and the natural frequency $\omega_0 = 7.6Hz$. In the region between the threshold curves $\lambda_2(1)$ and $\lambda_2(2)$, the Melnikov function changes sign and chaos occurs. Two different damping cases are chosen to visualize the responses to verify the prediction of chaos occurring. Both cases are compared with critical curves in Fig. 18.

Case 2 corresponds to the point situated above the threshold value, and the black phase trajectory of w is located around one of the equilibrium points within the pseudo-separatrix in Fig. 17. In this stage, the excitation is considered as low energy because it has a far larger nonlinear stiffness than that of cubic stiffness. As the damping parameter decreases to the chaos region, as in case 1, the displacement of NES crosses the two equilibrium points. The phase trajectory escapes from one potential well to the other, and the chaotic behaviours are identified in Fig. 18.

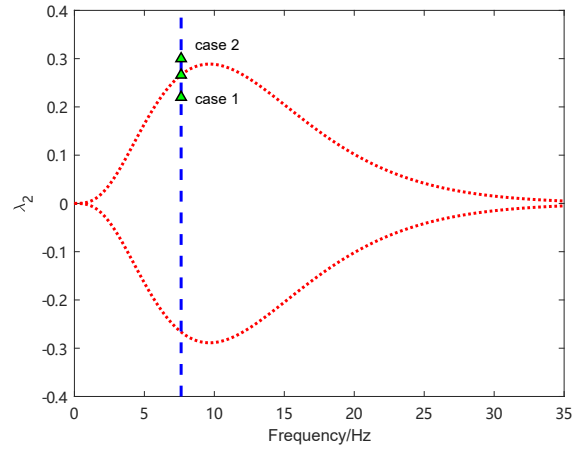


Fig. 17. Chaos boundary for λ_2 with designed amplitude $N_1 = 3mm$ ($\varepsilon = 0.01, K = 1754, \delta = -0.44$). The blue dashed line is the natural frequency ω_0 of the primary system

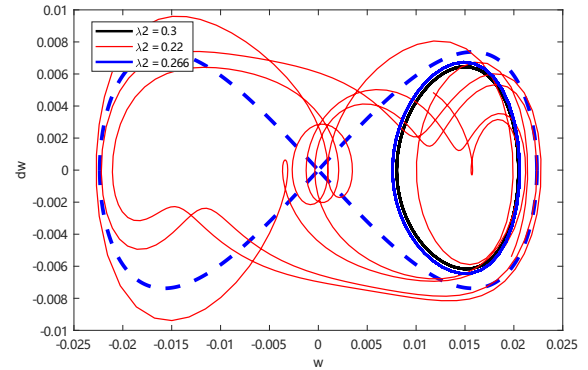


Fig. 18. Phase trajectory for different damping parameters λ_2 , black line: $\lambda_2 = 0.3$, intra-well oscillation; red line: $\lambda_2 = 0.266$, critical value for occurrence of chaos; blue line: $\lambda_2 = 0.22$, chaos inter-well oscillation

By setting the different N_1 amplitude requirements, the boundary of chaos can vary. It is clear from the figure 19 that the region of chaotic behaviour between the two surfaces becomes larger as N_1 increases. These conditions provide a domain in the parameter spaces, where the Melnikov function changes its sign and the possible chaotic behaviours happen. Meanwhile, the phase trajectory of NES will cross the pseudo-separatrix. According to the amplitude of LO, the result can predict and distinguish the formation of chaos and can be used for the optimal design of bistable NES systems.

5.2 Efficiency analysis of bistable NES

Fig. 20 illustrates the performance of bistable NES and its various stages with increasing excitation. The boundary of chaos (G_0c) can be obtained by the Melnikov method. Due to the mixture of chaos stage and beginning SMR, the analytical expression G_1c can not describe the occurrence of SMR. But the threshold excitation (G_2c) is still helpful for predicting the disappearance of SMR [19], which gives:

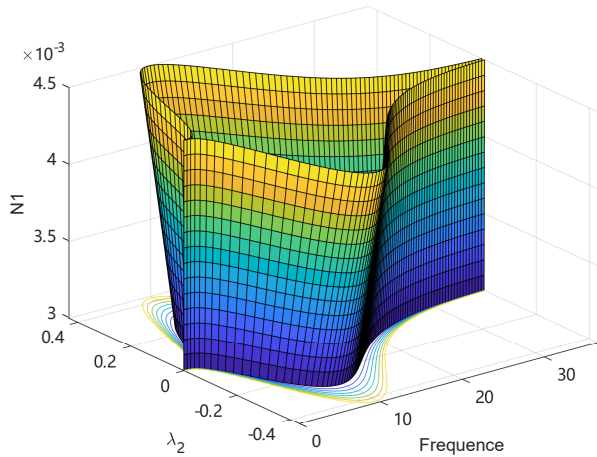


Fig. 19. Chaos boundary for λ_2 with different designed amplitude N_1 ($\varepsilon = 0.01, K = 1742, \delta = -0.44$)

$$\begin{aligned}
 G_{ic} &= \varepsilon \frac{N_{2i} F_1}{4 F_2}, i = 1, 2 \\
 F_1 &= 9K^2 N_{2i}^4 \lambda_1 + 24KN_{2i}^2 \delta \lambda_1 - 24KN_{2i}^2 \lambda_1 \\
 &\quad + 16\delta^2 \lambda_1 + 16\lambda_1 \lambda_2^2 - 32\delta \lambda_1 + 16\lambda_1 + 16\lambda_2 \\
 F_2 &= (9K^2 N_{2i}^4 + 24KN_{2i}^2 \delta - 24KN_{2i}^2 + 16\lambda_2^2 + 16(\delta^2 - 1)^2)^{\frac{1}{2}} \\
 Z_{2i} &= N_{2i}^2 \frac{4(2(1 - \delta) \mp \sqrt{(1 - \delta)^2 - 3\lambda_2^2})}{9K}
 \end{aligned} \tag{32}$$

The response regimes in Fig. 20 clearly show the intrawell oscillation and stable response, which are divided by the analytic prediction. Before it enters the chaos stage, the NES exhibits a small amplitude response of oscillation around one of the equilibria. In this stage, the amplitude of LO increases almost linearly and the curves of A_m and A_e coincide. However, the efficiency decreases rapidly with increasing excitation.

In the second stage, the displacement of NES starts to pass the two equilibria. The curves A_e and A_m separate in Fig. 20, and the distance becomes larger, which means that the amplitude is not constant. With the introduction of SMR, the distance between the A_e and A_m becomes constant, confirming that the energy pumping occupies the whole time. Moreover, the bistable NES performs a higher efficiency than that of cubic NES because of higher speed, and more significant stroke swept in the dynamic transition of negative stiffness.

Once the SMR disappears, the curves of the A_e and A_m coincide again. The efficiency of the NES reaches its maximum value, where the LO amplitude starts to increase with the growth of excitation amplitude. It is reasonable to believe that the energy-absorbing capability is saturated.

For a given amplitude of excitation G , it can be considered an upper threshold of excitation $G_{2c} = G$ to achieve

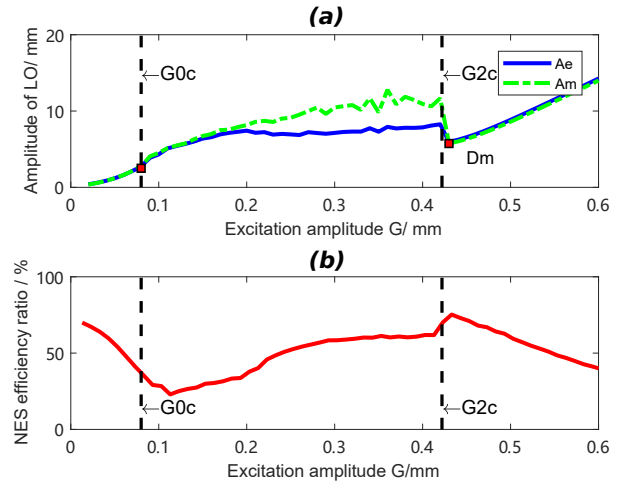


Fig. 20. Efficiency of bistable NES (a) the maximum amplitude (A_m) and mean amplitude (A_e) of LO for different excitation G ($\varepsilon = 0.01, \lambda_1 = 1.67, \lambda_2 = 0.167, K = 1754, \delta = -0.44$) (b) energy dissipation ratio of bistable NES. G_{0c} is the excitation threshold for chaos occurrence, G_{2c} is the excitation threshold for SMR disappear

maximum efficiency. Then, by substituting the last two equations into the first equation in Eqn. (32), the optimal stiffness expression K_m is determined. Since the expression for K_m is complex, it is presented in the appendix. In order to compare the numerical optimal stiffness with the analytical prediction (32) under the given fixed excitation, various nonlinear stiffnesses K are fully tested, and the result is presented in Fig. 21. The thick red line is the projection of minimum amplitude of LO in the $K - G$ plane. The thick blue line is the analytical prediction of K . The Fig. 21 illustrates an evident tendency that smaller nonlinear stiffness can bear larger excitation better. Without introducing the coefficient of correction, ξ , the analytical prediction can still describe the optimal $K - G$ curve with sufficient accuracy.

As with the efficiency analysis in the cubic case, the optimal point occurs in the stable response phase, where the SMR vanishes. The limit efficiency of the optimal point can be obtained from Eqn. (21), where the expressions of $Z_{2,1}$ and $Z_{2,2}$ are replaced by Eqn. (32). The following expression is the estimation of maximum efficiency for bistable NES.

$$r_{bis-NES} = \frac{9\lambda_2}{2\lambda_1\mu(\delta - 1 + \mu) + 12\lambda_1\lambda_2^2 + 9\lambda_2} \tag{33}$$

where $\mu^2 = \delta^2 - 3\lambda_2^2 - 2\delta + 1$.

Unlike Eqn. (22), the efficiency of bistable NES involves the negative stiffness. Eqn. (33) becomes the same as Eqn. (22), if $\delta = 0$. For example, the predicted value of maximum efficiency is 78% in Fig. 20. The maximum efficiency value obtained by direct calculation is 75%. So Eqn. (33) provides a simpler way to estimate the maximum efficiency of bistable NES.

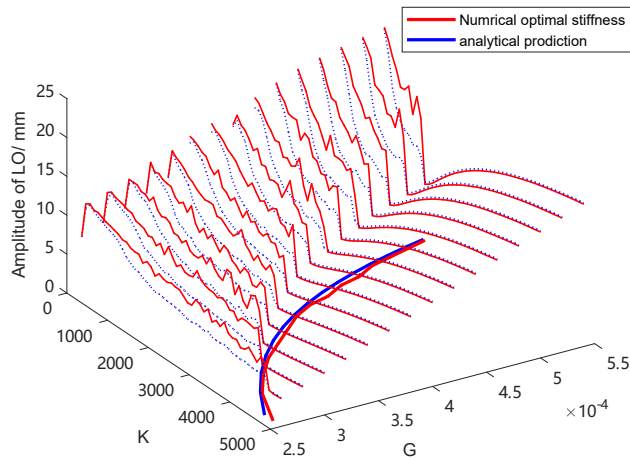


Fig. 21. Efficiency of bistable NES for different excitation G , where the nonlinear stiffness K is a control parameter ($\epsilon = 0.01, \lambda_1 = 1.67, \lambda_2 = 0.167, \delta = -0.44$)

5.3 Robustness analysis of optimal design method

In order to apply the optimal design in practice, it is essential to consider the effect of uncertainties of design parameters on the system response. This kind of uncertainties may come from the material properties and assembly errors of the system. The impact of these uncertainties on the performance of energy absorption, as well as on the reliability and robustness of the spring NES device are investigated in [33]. Under transient vibrations, the bistable NES has better robustness compared to tuned TMD. [34].

In a mechanical system, the negative and nonlinear stiffnesses are usually coupled. The value of K is chosen from 1250 to 2750, and δ varies from -0.56 to -0.3. Let the target harmonic excitation be fixed at $G = 0.4$ mm. According to the optimal nonlinear stiffness function in the appendix, one optimal value is obtained ($K = 2000, \delta = -0.43$), where the system has achieved the maximum efficiency of 75%. In the vicinity of the optimal design, an obvious dividing line is observed. The efficiency distribution shows a cut off on both sides of the separatrix (dashed line in Fig. 22), calculated using the optimal stiffness function found in the appendix.

For quantitative comparison of the stiffness uncertainties, the responses of two other parameters combinations on each side (case A: $K=1750, \delta = -0.5$ and case B: $K=2200, \delta = -0.41$) are also compared with the optimal design, which is presented in Fig. 22. In the left half part of the parameters plane, the designed system performs a SMR such as case A in Fig. 23. Although the LO has an unstable amplitude, it can be considered as efficient energy-absorbing, and the average efficiency can be 62%. In this region, the optimal design of the bistable NES shows strong robustness. A variety of K and δ ensures the occurrence of SMR and does not significantly change the efficiency (about 62%). If the negative stiffness is too low, it increases the duration of each SMR cycle and consequently induces a decrease in efficiency.

If the system parameters are located on the right side of

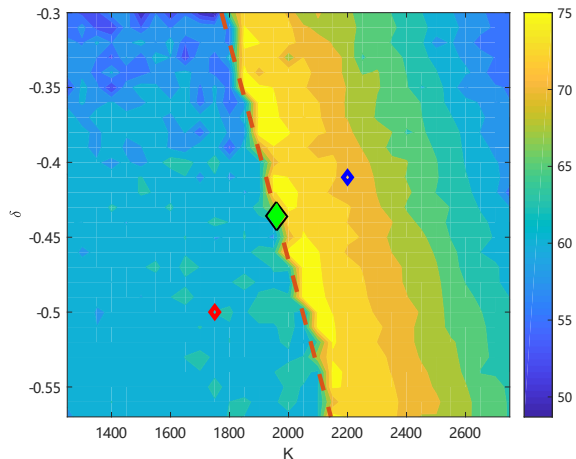


Fig. 22. Influence of design parameters $K - \delta$ on efficiency for excitation $G = 0.4$ mm. The green diamond corresponds to the optimal design with $K = 2000, \delta = -0.43$. Case A (red diamond): $K = 1750, \delta = -0.5$ and case B (blue diamond): $K = 2200, \delta = -0.41$

the dividing line, the capacity to absorb energy is saturated, and the response turns to be a periodic oscillation. The stable amplitude of LO is 5.9 mm in case B and it is slightly larger than 5.4 mm under optimal design in Fig. 23. In case B, the efficiency of NES is still considerably high. The system's efficiency is more sensitive to variation in nonlinear stiffness K . So the contour map of the efficiency distribution shows a striped form on the right part. In this region, the system's periodic response always possesses a higher efficiency than that of SMR. Once the optimal design is fixed, the chosen K (of the real system) should be slightly larger than the calculated value, in order to ensure a stable response. A descent of δ also helps stabilise the response and achieve high efficiency in the vicinity of the optimal design. Our optimal method allows to determine the minimal but optimal stiffness required for certain excitations.

6 Conclusion

The current study investigates the basic constraints on the maximum absorbing efficiency limit for the optimization of both cubic and bistable NES. Based on the response regimes, the optimal point is selected by considering the energy absorbing efficiency. Several main conclusions can be drawn:

1. The conservative system shows the same tendency as the non-conservative system according to the variety of negative stiffness and nonlinear stiffness. An increase in nonlinear stiffness leads the frequency-energy backbone of the conservative system to move to a lower energy level. This implies that the corresponding NES system can sustain a lower optimal energy input in a non-conservative system. A bistable NES with stronger negative stiffness can produce SMR over a wider range of excitation.

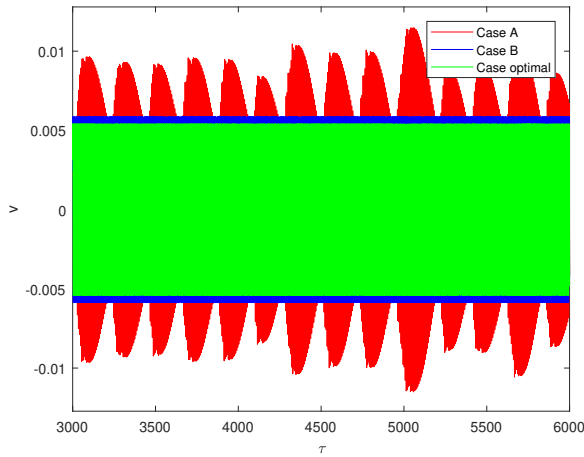


Fig. 23. Time-displacement of optimal case ($K = 1958$, $\delta = -0.44$), case A ($K=1750$, $\delta = -0.5$) and case B ($K=2200$, $\delta = -0.41$) for excitation $G = 0.4\text{mm}$

2. When the SMR occurs, the conservative energy level of the cubic NES system is always located at the saddle point of the $S11-$ branch. So this saddle point can be considered as a indication that SMR occurs. A simpler expression $\frac{8}{81K}$ can predict the critical threshold energy for triggering the SMR mechanism. The simulations in the case of different nonlinear stiffnesses confirm that the trigger energy level mainly depends on the K design. Moreover, a critical damping value λ_2 exists and governs the occurrence of chaotic behaviours under certain design.
3. The analytical relationship between the optimal K value and a certain excitation G has been given and verified by simulation. The error between the analytical $K - G$ relation and the numerical result can be reduced by introducing a correction coefficient ξ , which measures the distance of saddle point $Z_{2,2}$ from the simulated arrival point $Z_{2,a}$ in the cubic case.
4. The emergence of the maximum efficiency point is similar in the response regimes of both cubic and bistable NES. It appears during the transition from the SMR response to the stable response. Explained by SIM structure, the singular point $Z_{2,2}$ represents the maximum efficiency point that this system can achieve. Based on this characteristic, the expression of the maximum efficiency is found. The maximum efficiency value only depends on the damping parameters λ_1 and λ_2 in cubic case. The design of K determines the optimal absorbing excitation amplitude G only, without influencing the maximum efficiency level.
5. The performances of bistable NES cases, whose parameters are in the vicinity of optimal combination, are compared to verify their robustness. A slightly larger value of nonlinear stiffness than the calculated value can help the system achieve its target excitation both for cubic and bistable NES designs. The bistable NES can possess a strong robustness facing the uncertainties of K , as long

as K value is within the optimal interval. This practical strategy for choosing a proper combination of δ and K helps the system maintain its maximum efficiency value.

7 Appendix

Optimal nonlinear stiffness

$$K_m = \frac{2}{81} (\epsilon^2 (-144\delta\lambda_1^2\lambda_2^4 + 72\delta^2\lambda_1^2\lambda_2^2 - 36\delta^3\lambda_1\lambda_2 - 72\delta\lambda_1^2\lambda_2^2 - 324\delta\lambda_1\lambda_2^3) + 108\delta^2\lambda_1\lambda_2 - 108\delta\lambda_1\lambda_2 - 24\delta^3\lambda_1^2\lambda_2^2 + 48\mu\delta\lambda_1^2 + 108\mu\lambda_1\lambda_2^3 - 12\mu\delta^4\lambda_1^2 - 36\mu\lambda_1\lambda_2 + 48\mu\delta^3\lambda_1^2 - 24\mu\lambda_1^2\lambda_2^2 - 72\mu\delta^2\lambda_1^2 - 8\delta^5\lambda_1^2 + 40\delta^4\lambda_1^2 + 144\lambda_1^2\lambda_2^4 - 80\delta^3\lambda_1^2 + 80\delta^2\lambda_1^2 + 24\lambda_1^2\lambda_2^2 + 324\lambda_1\lambda_2^3 - 40\delta\lambda_1^2 - 162\delta\lambda_2^2 + 36\lambda_1\lambda_2 + 8\lambda_1^2 + 36\mu\lambda_1^2\lambda_2^4 + 162\lambda_2^2 - 12\mu\lambda_1^2 + 81\mu\lambda_2^2 + 4\mu^3\lambda_1^2 - 24\mu\delta^2\lambda_1^2\lambda_2^2 + 48\mu\delta\lambda_1^2\lambda_2^2 - 36\mu\delta^2\lambda_1\lambda_2 + 72\mu\delta\lambda_1\lambda_2 + 4\mu^3\delta^2\lambda_1^2 - 8\mu^3\delta\lambda_1^2)^2 / (G^2 (\delta^2 + \delta\mu + 3\lambda_2^2 - 2\delta - \mu + 1)) \quad (34)$$

where $\mu^2 = \delta^2 - 3\lambda_2^2 - 2\delta + 1$

References

- [1] Franchek, M., Ryan, M., and Bernhard, R., 1996. "Adaptive passive vibration control". *J.Sound Vib.*, **189**(5), pp. 565–585.
- [2] Vakakis, A. F., and Gendelman, O., 2001. "Energy pumping in nonlinear mechanical oscillators: part ii—resonance capture". *J.Appl Mech.*, **68**(1), pp. 42–48.
- [3] Kerschen, G., Lee, Y. S., Vakakis, A. F., McFarland, D. M., and Bergman, L. A., 2005. "Irreversible passive energy transfer in coupled oscillators with essential nonlinearity". *SIAM J.Appl Math*, **66**(2), pp. 648–679.
- [4] Gendelman, O., Manevitch, L., Vakakis, A. F., and M'closkey, R., 2001. "Energy pumping in nonlinear mechanical oscillators: part i—dynamics of the underlying hamiltonian systems". *J. Appl. Mech.*, **68**(1), pp. 34–41.
- [5] Lee, Y., Vakakis, A. F., Bergman, L., McFarland, D., Kerschen, G., Nucera, F., Tsakirtzis, S., and Panagopoulos, P., 2008. "Passive non-linear targeted energy transfer and its applications to vibration absorption: a review". *Proc.Inst.Mech Eng Part K-J Multi-body Dyn.*, **222**(2), pp. 77–134.
- [6] Starosvetsky, Y., and Gendelman, O., 2008. "Attractors of harmonically forced linear oscillator with attached nonlinear energy sink. ii: Optimization of a nonlinear vibration absorber". *Nonlinear Dyn.*, **51**(1-2), pp. 47–57.
- [7] Vaurigaud, B., Savadkoobi, A. T., and Lamarque, C.-H., 2011. "Targeted energy transfer with parallel nonlinear energy sinks. part i: design theory and numerical results". *Nonlinear dyn.*, **66**(4), pp. 763–780.
- [8] McFarland, D. M., Kerschen, G., Kowtko, J. J., Lee, Y. S., Bergman, L. A., and Vakakis, A. F., 2005. "Experimental investigation of targeted energy transfers in

- strongly and nonlinearly coupled oscillators”. *J.Acoust Soc Am.*, **118**(2), pp. 791–799.
- [9] Gourdon, E., Alexander, N. A., Taylor, C. A., Lamarque, C.-H., and Pernot, S., 2007. “Nonlinear energy pumping under transient forcing with strongly nonlinear coupling: Theoretical and experimental results”. *J.Sound Vib.*, **300**(3-5), pp. 522–551.
- [10] Bellet, R., Cochelin, B., Herzog, P., and Mattei, P.-O., 2010. “Experimental study of targeted energy transfer from an acoustic system to a nonlinear membrane absorber”. *J.Sound Vib.*, **329**(14), pp. 2768–2791.
- [11] Gourc, E., Michon, G., Seguy, S., and Berlioz, A., 2014. “Experimental investigation and design optimization of targeted energy transfer under periodic forcing”. *J.Vib Acoust.*, **136**(2), p. 021021.
- [12] Chen, Y.-Y., Qian, Z.-C., Zhao, W., and Chang, C.-M., 2020. “A magnetic bi-stable nonlinear energy sink for structural seismic control”. *J.Sound Vib.*, **473**, p. 115233.
- [13] Tian, W., Li, Y., Li, P., Yang, Z., and Zhao, T., 2019. “Passive control of nonlinear aeroelasticity in hypersonic 3-d wing with a nonlinear energy sink”. *J.Sound Vib.*, **462**, p. 114942.
- [14] Manevitch, L., 2001. “The description of localized normal modes in a chain of nonlinear coupled oscillators using complex variables”. *Nonlinear Dyn.*, **25**(1-3), pp. 95–109.
- [15] Starosvetsky, Y., and Gendelman, O., 2008. “Response regimes of linear oscillator coupled to nonlinear energy sink with harmonic forcing and frequency detuning”. *J.Sound Vib.*, **315**(3), pp. 746–765.
- [16] Romeo, F., Sigalov, G., Bergman, L. A., and Vakakis, A. F., 2015. “Dynamics of a linear oscillator coupled to a bistable light attachment: numerical study”. *J.Comput. Nonlinear Dyn.*, **10**(1), p. 011007.
- [17] Farshidianfar, A., and Saghafi, A., 2014. “Global bifurcation and chaos analysis in nonlinear vibration of spur gear systems”. *Nonlinear Dyn.*, **75**(4), pp. 783–806.
- [18] Guckenheimer, J., and Holmes, P., 2013. *Nonlinear oscillations, dynamical systems, and bifurcations of vector fields*, Vol. 42. Springer Science & Business Media, Berlin.
- [19] Qiu, D., Seguy, S., and Paredes, M., 2018. “Tuned nonlinear energy sink with conical spring: design theory and sensitivity analysis”. *J.Mech Des.*, **140**(1), p. 011404.
- [20] Silva, C. E., Maghareh, A., Tao, H., Dyke, S. J., and Gibert, J., 2019. “Evaluation of energy and power flow in a nonlinear energy sink attached to a linear primary oscillator”. *J.Vib Acoust.*, **141**(6), p. 061012.
- [21] Wei, Y., Peng, Z., Dong, X., Zhang, W., and Meng, G., 2017. “Mechanism of optimal targeted energy transfer”. *J.Appl Mech.*, **84**(1), p. 011007.
- [22] AL-Shudeifat, M. A., and Saeed, A. S., 2020. “Comparison of a modified vibro-impact nonlinear energy sink with other kinds of ness”. *Meccanica.*, pp. 1–18.
- [23] Masana, R., and Daqaq, M. F., 2011. “Relative performance of a vibratory energy harvester in mono-and bi-stable potentials”. *J.Sound Vib.*, **330**(24), pp. 6036–6052.
- [24] AL-Shudeifat, M. A., 2014. “Highly efficient nonlinear energy sink”. *Nonlinear Dyn.*, **76**(4), pp. 1905–1920.
- [25] Habib, G., and Romeo, F., 2017. “The tuned bistable nonlinear energy sink”. *Nonlinear Dyn.*, **89**(1), pp. 179–196.
- [26] Lee, Y. S., Kerschen, G., Vakakis, A. F., Panagopoulos, P., Bergman, L., and McFarland, D. M., 2005. “Complicated dynamics of a linear oscillator with a light, essentially nonlinear attachment”. *Phys.D Nonlinear Phenom.*, **204**(1-2), pp. 41–69.
- [27] Manevitch, L., Sigalov, G., Romeo, F., Bergman, L., and Vakakis, A., 2014. “Dynamics of a linear oscillator coupled to a bistable light attachment: analytical study”. *J.Appl Mech.*, **81**(4), p. 041011.
- [28] Romeo, F., Manevitch, L., Bergman, L., and Vakakis, A., 2015. “Transient and chaotic low-energy transfers in a system with bistable nonlinearity”. *Chaos.*, **25**(5), p. 053109.
- [29] Starosvetsky, Y., and Gendelman, O., 2010. “Interaction of nonlinear energy sink with a two degrees of freedom linear system: Internal resonance”. *J.Sound Vib.*, **329**(10), pp. 1836–1852.
- [30] Gendelman, O., Starosvetsky, Y., and Feldman, M., 2008. “Attractors of harmonically forced linear oscillator with attached nonlinear energy sink i: description of response regimes”. *Nonlinear Dyn.*, **51**(1-2), pp. 31–46.
- [31] Starosvetsky, Y., and Gendelman, O., 2010. “Bifurcations of attractors in forced system with nonlinear energy sink: the effect of mass asymmetry”. *Nonlinear Dyn.*, **59**(4), pp. 711–731.
- [32] Qiu, D., Li, T., Seguy, S., and Paredes, M., 2018. “Efficient targeted energy transfer of bistable nonlinear energy sink: application to optimal design”. *Nonlinear Dyn.*, **92**(2), pp. 443–461.
- [33] Braydi, O., Gogu, C., and Paredes, M., 2020. “Robustness and reliability investigations on a nonlinear energy sink device concept”. *Mech. Ind.*, **21**(6), p. 603.
- [34] Dekemele, K., Van Torre, P., and Loccufer, M., 2019. “Performance and tuning of a chaotic bi-stable nes to mitigate transient vibrations”. *Nonlinear Dyn.*, **98**(3), pp. 1831–1851.